Seismo-volcano source localization with triaxial broad-band seismic array

Adolfo Inza, Jerome Mars, Jean-Philippe Métaxian, Gareth S. O'Brien, Orlando Macedo

Geophys. J. Int. (2003) **000,** 000–000

Seismo-Volcano Source Localization with Triaxial-Broadband Seismic Array

L. A. Inza[1,2,4], J.I. Mars[1], J. P. Métaxian[2], G. S O'Brien[3] and O. Macedo[4]

[1] *GIPSA-LAB/DIS/UMR 5216 Institute Polytechnique de Grenoble, FRANCE*
[2] *Laboratoire de Géophysique Interne et Tectonophysique IRD:R157 CNRS, Université de Savoie, FRANCE*
[3] *School of Geological Science, University College Dublin IRELAND*
[4] *Instituto Geofisico del Peru, IGP PERU*

Received 2010 September 18; in original form 2010 September 5

SUMMARY

Seismo-volcano source localization is essential to improve our understanding of eruptive dynamics and of magmatic systems. The lack of clear seismic wave phases prohibits the use of classical location methods. Seismic antennas composed of one-component (1C) seismometers provide a good estimate of the back-azimuth of the wavefield. The depth estimation, on the other hand, is difficult or impossible to determine. As in classical seismology, the use of three component (3C) seismometers is now common in volcano studies. In order to determine the source location parameters (back-azimuth and depth), we extend the 1C seismic antenna approach to 3C's. This article discusses a high-resolution location method using a 3C array survey (3C MUSIC algorithm) with data from two seismic antennas installed on an andesitic volcano in Peru (Ubinas volcano). One of the main scientific questions related to the eruptive process of Ubinas volcano is the relationship between the magmatic explosive and LP swarms. After introducing the 3C array theory, we evaluate the robustness of the location method on a full wavefield 3D synthetic dataset generated using a digital elevation model of Ubinas volcano and a heterogeneous velocity model obtained from a tomography study. Results show that the back-azimuth determined using the 3C array has a smaller error than a 1C array. Only the 3C method allows the recovery of the source depths. Finally, we applied the 3C approach to a seismic event recorded in 2009. Crossing the estimated back-azimuth and incidence angles, we find a source located 1000 ± 250 m below the bottom the active crater. Therefore, extending 1C arrays to 3C arrays in volcano monitoring allows a more accurate determination of the source epicenter and now an estimate for the depth.

Key words: Spatial analysis, Volcan monitoring, Fourier analysis, Time series analysis, Seismic array analysis.

1 INTRODUCTION

Source location (back-azimuth and depth determination) is a fundamental goal in volcano monitoring. Long-period (LP) events and tremor, which are directly related to magma ascent, constitute the main classes of seismic events observed on andesitic volcanoes (Chouet, 1996). Locating these events is therefore necessary to better understand the eruptive dynamics and to improve the knowledge of the magmatic system. The lack of clear body-wave phase arrivals and emergent onsets in LP events and tremor makes locating these events extremely difficult using classical hypocenter determination methods based on phase picking and calculation of travel times. Other location methods have been used in recent years including a method based on the spatial distribution of seismic amplitudes to locate eruptive tremor sources on the Piton de la Fournaise volcano (Battaglia & Aki, 2003) and to track tremors produced by lahars on Cotopaxi volcano (Hiroyuki et al., 2009). Dense one-component (1C) array methods based on time delays between close sensors, hence an estimation of the slowness vector of the wavefronts propagating across the array, have been used by several authors and applied to a great variety of volcanoes. For example (Saccorotti & DelPezzo, 2000) and (La Rocca et al., 2004) applied dense one-component array techniques to locate explosive activity at Stromboli. (Almendros et al., 2002) characterized the spatial extent of a hydrothermal system at Kilauea volcano by using similar techniques. (Metaxian et al., 2002) used several small dense arrays to locate LP events and tremor sources at Arenal volcano and (Di Lieto et al., 2007) used two dense one-component arrays of short period seismometers to track volcanic tremor at Etna. Dense one-component array methods usually consist of only the vertical seismic component and allow a good estimation of the back-azimuth of the wavefield. Unfortunately, the depth estimation is poorly resolved because the incidence angle is very difficult to determine. To overcome this problem, triaxial sensors (3C) can be used. In

this work we focus on the gain in back-azimuth resolution and depth determination obtained by three-component rather than one-component seismometers. In our study two 3C arrays were installed on Ubinas volcano, Peru, in March 2009 in order to determine the back-azimuth and depth of the seismo-volcano sources. The two small-aperture cross-shaped seismic arrays consisted of 12 three-component broadband seismometers. One of the main scientific questions related to the eruptive process at Ubinas is the relationship between the magmatic explosions and the LP swarms preceding these events by several tens of minutes to a few hours (Macedo et al., 2009). Source location of the LP events with a higher resolution compared to the one component dense array methods, particularly in the depth determination, is the main objective of this work. To achieve this goal and before working with real wavefield data we performed several numerical simulations of seismic wave propagation using a 3D digital elevation map and heterogeneous velocity model determined from a tomography study, (Monteiller et al., 2005). Sources were placed at different depths below the crater and receivers are situated at the same positions as the two experimental cross-shaped arrays. A high-resolution method based on the multiple signal classification (MUSIC technique) (Bienvenu & Kopp, 1983), (Schmidt, 1986), but adapted to the 3C case, is applied to the synthetic data to determine the back-azimuth, the apparent velocity and the incidence angle for both arrays and all sources. This procedure is then applied to the real data recorded in March 2009.

2 UBINAS VOLCANO

Ubinas volcano (16 22' S, 70 54' W; altitude 5672 m) began to erupt on March 25^{th} 2006 after nearly 40 years of quiescence. Situated in the Central Volcanic Zone (CVZ, southern Peru), Ubinas volcano is an active andesitic stratovolcano (De Silva & Francis, 1991) truncated in the upper part by a caldera 600 m in diameter. The caldera floor is a flat area lying approximately 5100 m above sea level. The active crater is situated in the southern section; the bottom is 300 m under the caldera floor (Figure 1a). Ubinas is considered the most active Peruvian volcano during the last 500 years, threatening 3,500 people living on the edge of the Ubinas rio (Rivera et al., 1998). Arequipa airport, situated 60 km east of the volcano, has been closed several times since 2006 due to ash emissions. The Instituto Geofisico del Peru (IGP) with the cooperation of the Institut de Recherche pour le Developement (IRD) has started seismic monitoring of the volcano to understand the activity associated with this eruptive sequence under the 6^{th} framework EU project VOLUME (http://www.volume-project.net/). A network of four digital 1 Hz stations with a radio telemetry system has been operating since 2006. Data are transmitted to Arequipa observatory. At the time of the experiment, the eruption was characterized by an almost permanent ash emission. Two main types of degasification were observed: 1) exhalations rising a few hundred meters above the crater rim and 2) plumes produced by explosions that may reach 10 km, critical for aircraft duty. This activity is thought to be related to a magmatic plug positioned at the bottom of the south part of the caldera wall (Macedo et al., 2009).

3 PROCESSING APPROACH

Three component broadband seismic array data is suitable for wide-band multidimensional signal processing techniques. The antenna is designed (size, shape, aperture) to avoid spatial and temporal aliasing (Mars et al., 2004). To illustrate the 3C MUSIC method, we assume an isotropic source radiation pattern and a homogeneous medium. Assuming K sources impinging at the antenna of N triaxial sensors, equation (1) represents the received signal by n^{th} sensor in time-space $(t-x)$ domain.

$$x_n(t) = \sum_{k=1}^{K} s_k(t-\tau_{n,k}) + b_n(t); \quad n = 0, 1, ..., N-1 \qquad (1)$$

where, $s_k(t)$ is the k^{th} source signal received in the first sensor, the $\tau_{n,k}$ is the relative propagation time delay of k^{th} source for the n^{th} sensor and the $b_n(t)$ represents the noise in n^{th} sensor (we assume white noise and Gaussian with variance σ^2 and uncorrelated with the sources). The corresponding relative time delay is defined as $\tau_{n,k} = \frac{1}{v_0}[\mathbf{r_n} \cdot \mathbf{u}(\theta_k, \phi_k)]$ where, v_0 is the wave propagation apparent velocity beneath the array, the $\mathbf{r}_n$ is the relative location for sensor n^{th} respect to the first sensor located at (0,0,0) and the $\mathbf{u}(\theta_k, \phi_k)$ is the slowness vector of the impinging wavefield from k^{th} source. The dot product $(\mathbf{r_n} \cdot \mathbf{u})$ represents the propagation path between the n^{th} sensor respect to the first sensor. The propagation direction $\mathbf{u}(\theta_k, \phi_k)$ of the k^{th} source arrived in the antenna can be described by back-azimuth angle θ_k and vertical incidence angle ϕ_k, these two parameters are combined in the slowness vector as is shown in equation (2).

$$\mathbf{u}(\theta_k, \phi_k) = \begin{bmatrix} -sin\theta_k sin\phi_k \\ -cos\theta_k sin\phi_k \\ cos\phi_k \end{bmatrix} \qquad (2)$$

Taking into account the wavenumber $\mathbf{k}$, that is related as $\mathbf{k} = \frac{1}{\lambda_w}\mathbf{u} = \frac{f_o}{v_o}\mathbf{u}$, where, λ_w is the wavelength, f_o the wave frequency and v_o is the wave propagation apparent velocity. The Fourier transform in equation (1) can be represented in the frequency-wavenumber $(f-k)$ domain as:

$$X_n(f_o) = \sum_{k=1}^{K} S_k(f_o) exp(-2\pi j \mathbf{r_n} \cdot \mathbf{k}) + B_n(f_o) \qquad (3)$$

where, $j = \sqrt{-1}$ is the imaginary unit, and $S_k(f)$ and $B_n(f)$ are the Fourier transform of $s_k(t)$ and $b_n(t)$ respectively. Then the antenna output $X(f_o)$ for narrowband signals can be represented as a Nx1 matrix form as:

$$X(f_o) = A(f_o) \cdot S(f_o) + B(f_o) \qquad (4)$$

where, the NxK matrix $A(f_o)$ is called "array reponse" or "steering matrix", the Kx1 matrix $S(f_o)$ keeps the sources signals defined in (5), so the Nx1 matrix $B(f_o)$ represents the noise.

$$A(f_o) = [\mathrm{a}(\theta_1, \phi_1), \mathrm{a}(\theta_2, \phi_2), ..., \mathrm{a}(\theta_K, \phi_K)] \qquad (5)$$

$$\mathrm{a}\,(\theta, \phi) = \begin{bmatrix} 1 \\ exp(-j2\pi \mathbf{r}_1 \cdot \mathbf{k}) \\ ..... \\ exp(-j2\pi \mathbf{r}_{N-1} \cdot \mathbf{k}) \end{bmatrix}$$

$$S(f_o) = [s_1(f_o), ..., s_K(f_o)]^T$$

Note that the array manifold a (θ, ϕ) depends on the frequency f_o of the signal through the wavenumber $\mathbf{k}$. The purpose of this paper is to develop and test a 3C MUSIC algorithm in order obtain a more robust estimation of the back-azimuth angle θ and a reliable incidence angle ϕ related to source depth determination.

3.1 3C MUSIC algorithm

MUltiple SIgnal Classification is an eigenstructure subspace analysis method, that is widely used in geophysics, particularly to enhance the signal-to-noise ratio. MUSIC algorithm tries to find the array manifold orthogonal to the noise subspace since the noise subspace is orthogonal to the signal subspace (Mars et al., 2004). A time window array data is selected, correspondig to either explosion quakes or LP events. A way to find out the dominants frequencies in the wavefield is through average energy spectrum of each component, which the analysis frequency f_o is determined. Observing M frequencies snapshots around the bin f_o (energy peak) are used to estimate the cross-spectral matrix. The i^{th} snapshot data is shown in equation (6) defined by a NxM matrix (Paulus & Mars, 2006).

$$\mathbf{X}_i = \begin{bmatrix} WE_{i,1} & SN_{i,1} & Z_{i,1} \\ \cdot & \cdot & \cdot \\ \cdot & \cdot & \cdot \\ WE_{i,N} & SN_{i,N} & Z_{i,N} \end{bmatrix}; \quad i = 1, ..., M \tag{6}$$

where, the triaxial sensor is represented by: the west-east component as WE, south-north as SN and vertical as Z. The cross-spectral matrix $\widehat{\mathbf{\Gamma}}$ can be estimated using the equation (7) (Paulus et al., 2005) and .

$$\widehat{\mathbf{\Gamma}}_x = \frac{1}{M} \sum_{i=1}^{M} \mathbf{X}_i \cdot \mathbf{X}_i^H \tag{7}$$

where ^{H} denotes conjugate transpose. The cross-spectral matrix in (7) can be expressed in terms of its N eigenvalues and eigenvectors (N=sensors number), as shown the equations (8).

$$\widehat{\mathbf{\Gamma}}_x(\nu) = \sum_{n=1}^{N} \lambda_n \mathbf{v_n} \cdot \mathbf{v_n^H} \tag{8}$$

where, λ_n and $\mathbf{v_n}$ are the n^{th} eigenvalue and eigenvector respectively. Anyway the sample cross-spectral matrix is the expected value of the outer product of the data vector. Using the orthogonality property between signal and noise subspaces, in the equation (4), the cross-spectral matrix $\mathbf{\Gamma}_x$ can be written as:

$$\mathbf{\Gamma}_x = \boldsymbol{A} \cdot \mathbf{E}\{\mathbf{S} \cdot \mathbf{S}^H\} \cdot \boldsymbol{A}^H + \mathbf{E}\{\mathbf{B} \cdot \mathbf{B}^H\} \tag{9}$$

$$\mathbf{\Gamma}_x(f_o) = \boldsymbol{A}(f_o)\, \mathbf{\Gamma}_s(f_o)\, \boldsymbol{A}^H(f_o) + \sigma_B^2(f_o)\, \mathbf{I}$$

where, $\mathbf{E}\{\cdot\}$ the expected operator, $\mathbf{\Gamma}_s(f_o)$ is the signal cross-spectral matrix, $\mathbf{I}$ is the identity matrix and σ_B^2 is the variance of the Gaussian white noise. This decomposition can be split into two orthogonal subspaces such as signal and noise. In this case the cross-spectral matrix (9) is equal to the estimated cross-spectral matrix in (7) and (8). Due to errors in the estimated cross-spectral matrix, the eigenvalues of the noise subspace are no longer equal to σ_B^2. Assuming K sources impinging the antenna of N sensors ($K < N$), the eigenvectors whose eigenvalues are the K largest eigenvalues define the signal subspace and the remaining N-K eigenvectors define the noise subspace. The largest eigenvalues are easily distinguishable from the rest in the eigenvalues λ_i, as $\lambda_1 \geq ... \geq \lambda_K \geq \lambda_{K+1} > ... > \lambda_N \approx \sigma^2$ shows the appropriate dimension of noise subspace on the $N - K$ smallest. Then the noise projector is defined by (Miron et al., 2005):

$$\mathbf{\Pi}^{\perp} = \sum_{k=K+1}^{N} \mathbf{v}_k \mathbf{v}_k^H$$

and the MUSIC estimator is (Wong & Zoltowski, 2000):

$$\mathbf{3CMUSIC}(\theta, \phi) = \frac{1}{\mathbf{A}^H(\theta, \phi)\, \mathbf{\Pi}^{\perp} \mathbf{A}(\theta, \phi)} \tag{10}$$

Then 3C MUSIC algorithm follows the procedure: 1) Selection by time windowing data for either a quake explosion or LP event. 2) Average power spectra density to determine the frequencies bins and entimate the cross-spectral matrix. 3) Eigen structure analysis to estimate the noise sub-space to build the noise projector. 4) Evaluate the 3C MUSIC estimator on slowness grid and velocity grid where the estimator is maximum.

4 DATA

A seismic experiment was carried out at Ubinas volcano between May and July 2009. We deployed two cross-shaped antennas with triaxial-broadband seismometers as depicted in Figure 1a. NUBI antenna was installed on a flat area 4632 m above sea level. It consists of twelve Guralp CMG-6TD seismometers (see reference for Guralp manual). WUBI antenna was installed on a sloping area from 4752 m to 4883 m above sea level. It consists of six Guralp CMG-6TD and six GEOMAX seismometers (see reference for Geomax manual) both with 24 bit seismic recorders (dynamic range 120 dB) and high accuracy time synchronization, GPS-based. The acquisition performed continuous recording with a sampling frequency of a 100 Hz. The horizontal components of such seismometers were oriented to geographical coordinates West-East (E component) and South-North (N component) respectively. The distances between seismometers was set to approximately 50 meters. Each seismometer location was surveyed by Trimble GPS (GeoXH, accuracy 0.3 m). Twelve explosion quakes and hundreds of LP events were recorded during the experiment. A synthetic dataset was generated to test the accuracy of the location methods. The synthetic dataset was created using a digital elevation map of Ubinas topography and the 2009 experimental array locations. A 3D discrete numerical elastic lattice method (O'Brien & Bean, 2004) was used to propagate waves in the structure with six broadband isotropic sources (Figure 1b) located beneath the summit. The velocity structure was generated from a tomography study (Monteiller et al., 2005) assuming a density of 2300 kg/m^3. The sampling frequency was fixed to 250 Hz.

4.1 Synthetic data analysis

To investigate the performance of the 3C MUSIC technique, we applied it to our synthetic dataset. For source number 3 (Figure 1b) and the synthetic array NUBI a one second time window including the first arrival was selected, Figure 2a. In order to find the dominant frequency, we averaged the power spectral density computed for the selected time window of each component and for each receiver. The dominant energy peak is located at 2.23 Hz (Figure 2b). The cross-spectral matrix was then calculated by using 32 windows around the bin. The eigendecomposition of the cross-spectral matrix gave us an overview of the signal-to-noise subspaces, by sorting the eigenvalues. In the first stage, we determined the eigenvectors corresponding to the noise subspace, which gives the projector. In the second stage, we calculated the steering vector which consists of the slowness vector estimated between 0 and 2π with steps of 3.6°. Given the projector and the steering vector, we obtained the 3C MUSIC spectrum represented in Figure 3a. The maximum

amplitude of the spectrum gives the back-azimuth and the velocities. The largest estimator point is located at 181 $\pm 3^\circ$ for the back-azimuth and 2900$\pm$75 m/s for the velocity. The vertical and horizontal cross-section of the 3C MUSIC spectrum are shown in Figures 3b and 3c. The incidence angle is deduced from the estimated values, back-azimuth and velocity. We found 85.5$\pm 6^\circ$ as shown in Figure 3d. The errors are estimated by taking the peak width of 95% of the maximum amplitude. These values agree well with the theoretical values.

We applied the same analysis to the synthetic data generated for both arrays and for all six sources. In order to compare the 3C and 1C methods, we also analyzed the same synthetic dataset using only the vertical components. The results are shown in the Figure 4a and Figure 4b for NUBI and WUBI antennas respectively. Back-azimuth results obtained both with the 3C MUSIC and the 1C MUSIC fit well with the theoretical values for both antennas. Errors are $\pm 3^\circ$ and $\pm 6^\circ$, with the 3C and the 1C MUSIC algorithm respectively. However, the incidence angles are significantly different when using the 3C MUSIC and the 1C MUSIC analysis. For NUBI, values vary from 75° for the deepest source to 93° for source 1. These incident angle variations are coherent with the variation of the sources depth. Errors are $\pm 6^\circ$ for the 3C MUSIC analysis. These errors allow us to distinguish sources depths separated by several hundreds of meters but unable to separate close sources such as 1 and 2 or sources 4 and 5. The 1C MUSIC analysis gives sources close to the theoretical values for the superficial sources (1, 2 and 3) while depths for sources 4, 5 and 6 are far away from the theoretical values. The incident angle remains approximately the same value around 90°. The error obtained with the 1C MUSIC processing is $\pm 12^\circ$. None of the sources can be distinguished with the 1C MUSIC analysis. For WUBI antenna, the 3C MUSIC analysis gives incident angles between 63° for source 6 and 100° for source 2 (Figure 4b). As for NUBI, solutions follow the depth variation. Error are approximately 6°. The 1C MUSIC analysis gives higher incident angles than the theoretical values (90° for source 6 to 156° for source 1). Errors are larger than the 3C algorithm at approximately $\pm 15^\circ$. The 1C MUSIC analysis does not give reliable solutions for any of the synthetic source depths. In this case, it seems that the solutions are affected by the topography below the antenna. Similar results are observed for the velocity. In summary, incident angles obtained by the 3C MUSIC algorithm are close to the theoretical values whereas those obtained with 1C MUSIC are not reliable.

4.2 Real Data Analysis

In this section, we discuss the performance of 3C MUSIC method by applying it to an explosion quake signal recorded at Ubinas volcano. The selected event, recorded at 01:27 PM, June 2^{nd}, 2009 is shown in Figure 2c (SHOW A LONGER TIME WINDOW OF THE SIGNAL). The data was corrected for the instrument response and bandpass filtered between 1 Hz - 10 Hz. Figure 2d shows the antenna energy spectrum average obtained from two seconds of signal including the first arrival wave. The dominant peak is centred at 2.39 Hz. The results for NUBI antenna are presented in Figure 3e, 3f, 3g and 3h). (IF YOU WANT TO SEND TO DIFFERENT JOURNAL I'D SEPARATE THE SYNTHETIC AND DATA FIGURES) The maximum of the 3C MUSIC spectrum gives a back-azimuth of 184$\pm 5^\circ$, a velocity of 2975$\pm$125 m/s and an incidence angle of 85.9$\pm 7^\circ$. For WUBI, we obtained a back-azimuth of 119$\pm 6^\circ$, a velocity of 3100$\pm$120 m/s and an incidence angle of 75$\pm 7^\circ$. The back-azimuth and the incident angle can be represented as gaussian variables with mean θ ($0 \leq \theta \leq 360^\circ$) and ϕ ($0 \leq \phi \leq 120^\circ$) and standard deviations σ_θ and σ_ϕ corresponding to the values found in the analysis. This allows the definition of a probability density function (PDF) $\rho(\theta^k)$ of the back-azimuth and a PDF $\rho(\phi^k)$ of the incident angle for each array k. $\rho_1(\theta^k)$ and $\rho_1(\phi^k)$ are shown in Figure 5 as rose diagrams in the horizontal plane for the back-azimuths and in the vertical planes oriented N-S and W-E for the incident angle. The last step is to locate the source by using the information obtained at each antenna. For each point with geographical coordinates (x,y,z) in the source region and each array k, the back-azimuths $\theta^k(x,y,z)$ and the corresponding value of $\rho_1(\theta^k)$, as well as the incident angle $\phi^k(x,y,z)$ and the corresponding value of $\rho_1(\phi^k)$ can be calculated. The PDF of the source position is derived from the different PDF's of the back-azimuth and the incident angle:

$$\rho_2(x,y,z) = \prod_{k=1}^{2} \rho_1(\theta^k(x,y,z)) \cdot \rho_1(\phi^k(x,y,z)) \qquad (11)$$

The maximum likelihood of the PDF ρ_2 yields an estimate of the source location. We define the mean quadratic radius R = $\sqrt{(\sigma_1^2+\sigma_2^2+\sigma_3^2)/3}$, where σ_1^2, σ_2^2 and σ_3^2 are the principal variances of $\rho_2(x,y,z)$. Figure 5 shows the result obtained with the explosion quake analysis. The source area is situated 150 m West and 1000 m below the bottom of the crater at an altitude of 4200 m, the radius R is 660 m.

5 CONCLUSIONS

We have presented a source localization method, 3C MUSIC, based on the use of 3 component arrays and, for comparison, with the 1C MUSIC used in previous studies on volcanoes (Saccoroti et al. (2006)). Synthetics have been generated for 6 sources with elevations from 3400 m to 4950 m a.s.l. The back-azimuths from the 3C MUSIC correspond to the theoretical values for both antennas with a resolution of $\pm 3^\circ$. 1C MUSIC gives equivalent results, but with higher errors ($\pm 6^\circ$). The incident angle varies with depth when it is determined with 3C MUSIC. The incident angle is determined with an error of $\pm 6^\circ$ for NUBI and for WUBI. Knowing the distance from the center of the antennas and the hypocenter of the sources, depth resolution can be deduced for each antenna. It is 500 m for NUBI and 400 m and WUBI. On the other hand, the 1C MUSIC analysis does not allow the depth to be determined. It seems that the topography affects the results obtained with the 1C MUSIC. The velocity follows the same behaviour as the incident angle. The theoretical velocity has an accuracy of $\pm$150 m/s using the 3C MUSIC algorithm. The 1C MUSIC measures higher velocities at NUBI and lower velocities at WUBI. Finally, we located an explosion quake recorded during the field experiment using the 3C MUSIC. This signal is characteristic of the explosive activity observed at Ubinas volcano (Macedo et al. (2009)). We found a source located at 4200$\pm$500 m a.s.l. It is situated more than 1000 m below the summit of the intrusive conduit. We conclude that 3C MUSIC provides realistic values of the depth of volcanic sources, unlike the 1C MUSIC or other antenna methods based on time delays measurements. Given the performance of the 3C MUSIC algorithm, we will apply it to other explosions and other types of volcanic signals (LP, tremors) recorded at Ubinas to better characterize the eruptive dynamics of this volcano. In addition, the 3C MUSIC will be tested with the IGP monitoring system to try to locate the seismic activity in real time. This algorithm is not restricted to volcanic sources but can be used to locate other types of non-volcanic signals.

References

Almendros, J., Chouet, B., Dawson, P., & Huber, C., 2002. Mapping the sources of the seismic wave field at kilauea volcano, hawaii, using data recorded on multiple seismic antennas, *Bulletin of the Seismological Society of America*, **92**, 2333–2351.

Battaglia, J. & Aki, K., 2003. Location of seismic events and eruptive fissures on the piton de la fournaise volcano using seismic amplitudes, *Journal of Geophysical Research*, **108**, 2364, 14 PP.

Bienvenu, G. & Kopp, L., 1983. Optimality of high resolution array processing using eigensystem approach, *IEEE-ASSP*, **33**, 1235–1247.

Chouet, B., 1996. Long-period volcano seismicity: Its source and use in eruption forecasting, *Nature*, **380**, 309–316.

De Silva, S. & Francis, P., 1991. Volcanoes of the central andes, *Geological Magazine - Cambridge University Press*, **129**, 253–254.

Di Lieto, B., Saccorotti, G., L., Z., La Rocca, M., & Scarpa, R., 2007. Continuous tracking of volcanic tremor at mount etna, italy, *Geophysical Journal International*, **169**, 699–705.

Hiroyuki, K., Pablo, P., Takuto, M., Diego, B., & Masaru, N., 2009. Seismic tracking of lahars using tremor signals, *Journal of Volcanology and Geothermal Research*, **183**, 112–121.

La Rocca, M., Saccorotti, G., Del Pezzo, E., & Ibanez, J., 2004. Probabilistic source location of explosion quakes at stromboli volcano estimated with double array data, *Journal of Volcanology and Geothermal Research*, **131**, 123–142.

Macedo, O., Metaxian, J., Taipe, E., Ramos, D., & Inza, A., 2009. Seismicity associated with the 2006-2008 eruption ubinas volcano, *The Volume Project (VOLcanoes Understanding subsurface mass moveMEnt)*, **1**, 262–270.

Mars, J., Glangeaud, F., & Mari, J., 2004. Advanced signal processing tools for dispersive waves, *Near Surface Geophysics*, **2(4)**, 199–210.

Metaxian, J.-P., P. Lesage, & Valette, B., 2002. Locating sources of volcanic tremor and emergent events by seismic triangulation, *Geophys Researh Letters*, p. 107.

Miron, S., Bihan, N. L., & Mars, J., 2005. Vector-sensor music for polarized seismic sources localization, *EURASIP Journal on Applied Signal Processing*, **2005**, 74–84.

Monteiller, V., Got, J.-L., Virieux, J., & Okubo, P., 2005. An efficient algorithm for double-difference tomography and location in heterogeneous media, with an application to the kilauea volcano., *Journal of Geophysical Research B*, **110**, B12306.

O'Brien, G. S. & Bean, C. J., 2004. A 3d discrete numerical elastic lattice method for seismic wave propagation in heterogeneous media with topography, *Geophysical Research Letters*, **31**.

Paulus, C. & Mars, J., 2006. New multicomponent filters for geophysical data processing, *IEEE Geosciences and Remote sensing*, **44**, 2260–2270.

Paulus, C., Mars, J., & Gounon, P., 2005. Wideband spectral matrix filtering for multicomponent sensors array, *Signal Processing*, **85**, 1723–1743.

Rivera, M., Thouret, J.-C., & Gourgaud, A., 1998. Ubinas, el volcan mas activo del sur del peru desde 1550: Geologia y evaluacion de las amenazas volcanicas., *BolSocGeol Peru*, **88**, 53–71.

Saccoroti, G., Lieto, B. D., Tronca, F., Fischione, C., Scarpa, R., & Muscente, R., 2006. Performances of the underground seismic array for analysis of seismicity in central italy, *Annals of Geophysics*, **49**, 1041–1057.

Saccorotti, G. & DelPezzo, E., 2000. A probabilistic approach to the inversion of data from a seismic array and its application to volcanic signals, *Geophysical Journal International*, **143**, 249–261.

Schmidt, R., 1986. Multiple emitter location and signal parameter estimation, *IEEE Transactions Antennas and Propagation*, **34(3)**, 276–280.

Wong, K. T. & Zoltowski, M. D., 2000. Self-initiating music direction finding & polarization estimation in spatio-polarizational beamspace, *IEEE Transactions on Antennas and Propagation*, **48**, 671–681.

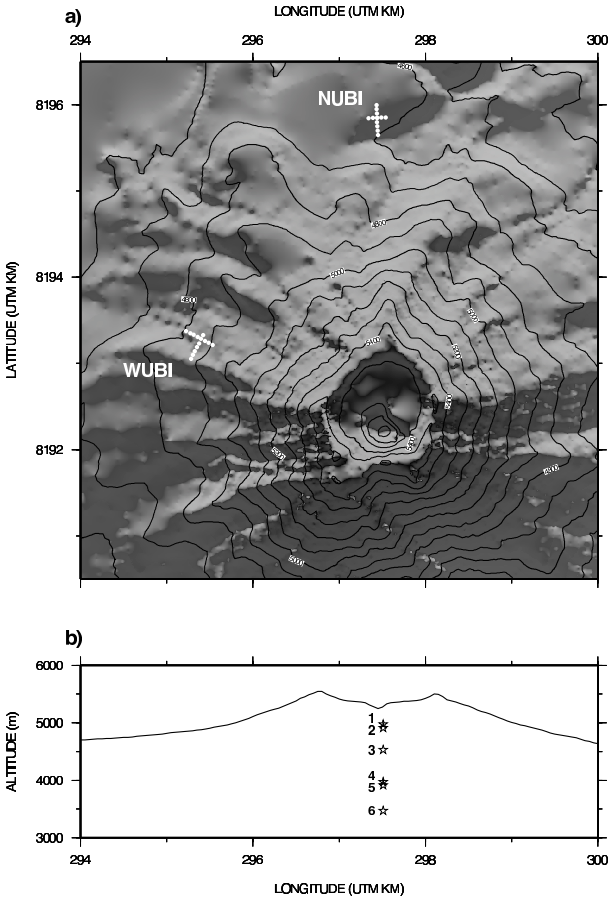

Figure 1. a) Map of Ubinas volcano showing the location of the north (NUBI) and the north-west (WUBI) antennas, b) Horizontal profile showing the position of the synthetic sources

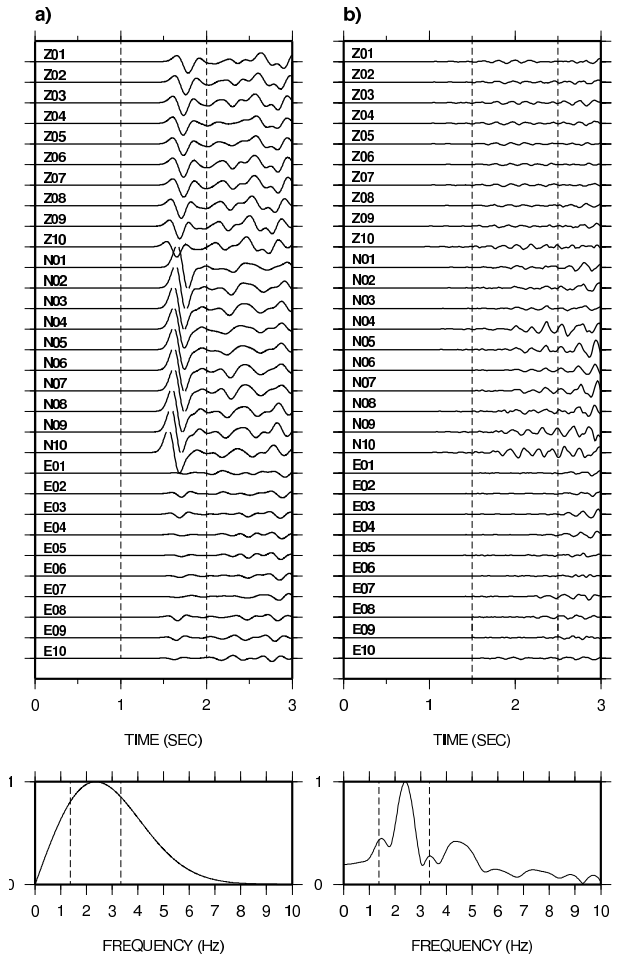

Figure 2. a) The vertical (Z), south-north (N) and west-east (E) synthetic seismograms calculated at the central receiver of NUBI antenna, b) Averaged energy spectrum calculated for all the receivers and all the components, c) The vertical (Z), south-north (N) and west-east (E) explosion-quake event waveforms (real data) recorded by the central receiver of NUBI antenna, d) Averaged energy spectrum calculated for all the receivers and all the components. The vertical dash lines in a) and c) indicate the time window (P-wave) selected for the processing. The vertical dash lines in c) and d) represent the frequency windows used for the cross spectral matrix calculation.

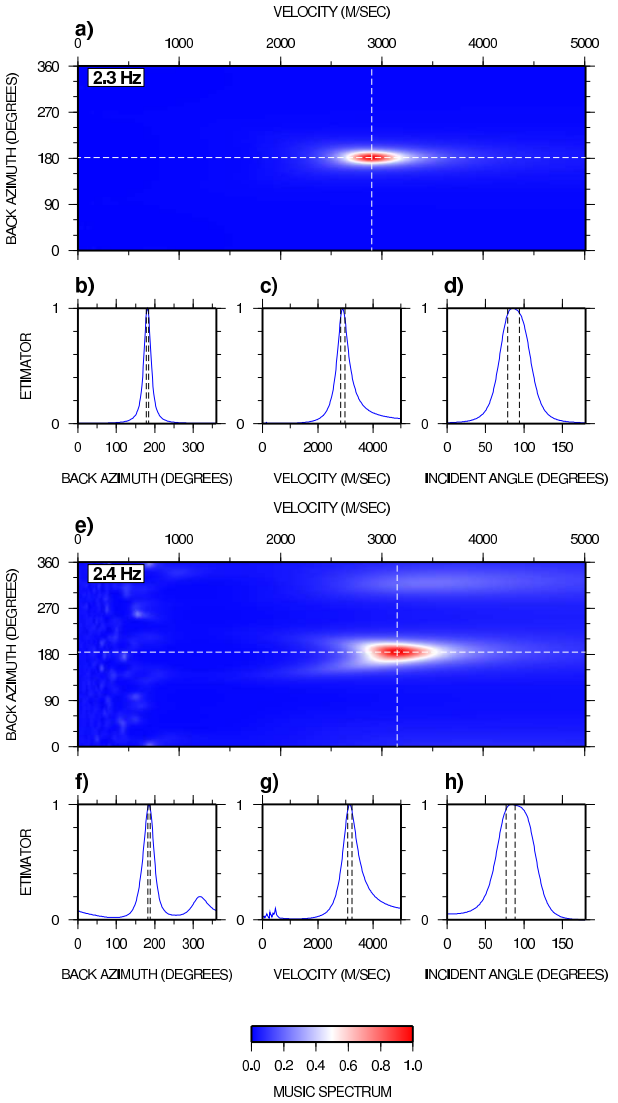

Figure 3. Results obtained for the synthetic data calculated for the six sources. Open triangles and open stars represent results obtained with the 3C MUSIC and 1C MUSIC, respectively. Results obtained for an explosion quake (real data) using the 3C MUSIC is represented by a closed circle. The abscissa represents the altitude. Sources are numbered as in figure 1b. a) Back-azimuth, incidence angle and velocity for NUBI antenna. b) Back-azimuth, incidence angle and velocity for WUBI antenna. Dash lines represent the theoretical values.

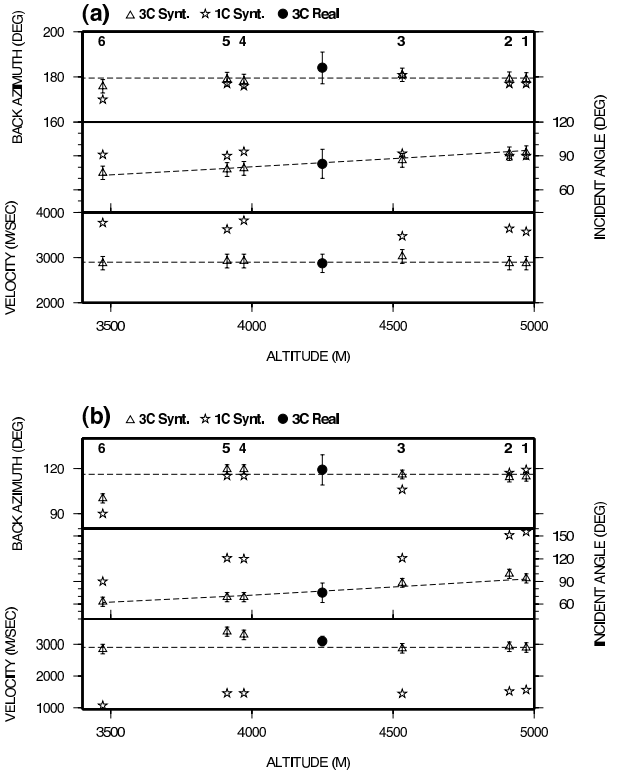

Figure 4. a) Normalized 3C MUSIC sprectrum calculated with syntetic data generated at source 3 for NUBI antenna. b) Normalized back-azimuth profile (cross section at velocity 2900 m/s). c) Normalized velocity profile (cross section at back-azimuth at 181 degrees). d) Normalized Incidence angle. e) Normalized 3C MUSIC spectrum for explosion-quake event. f) Normalized back-azimuth profile (cross section at velocity 2925 m/s). g) Normalized velocity profile (cross section at back-azimuth at 184 degrees). h) Normalized Incidence angle. The vertical dot lines represent the error range.

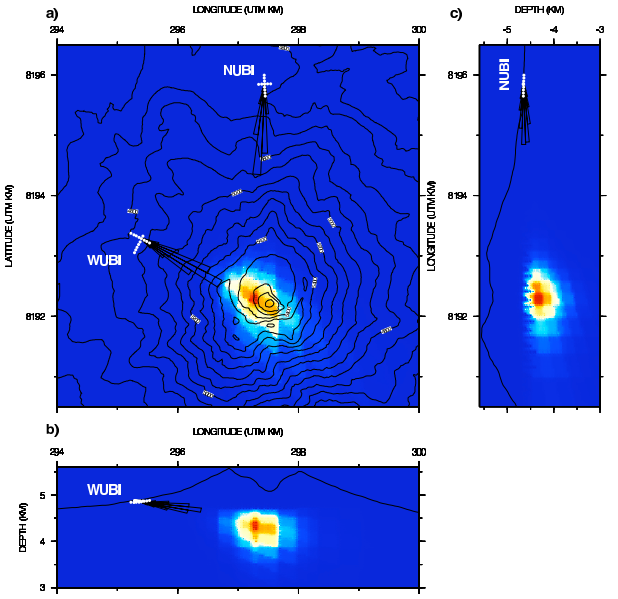

Figure 5. Probability density function of the source position ρ_2. a) horizontal view at 4200 m depth, b) vertical view oriented West-East crossing the maximum likelihood of ρ_2, c) same as b) oriented North-South. The PDF $\rho_1(\theta^k)$ and $\rho_1(\phi^k)$ are represented as rose diagrams with an increment of $5°$